bioRxiv preprint doi: https://doi.org/10.1101/368829; this version posted July 13, 2018. The copyright holder for this preprint (which was not certified by peer review) is the author/funder. All rights reserved. No reuse allowed without permission.

Reconstruction of the Decidual Pathways in Human Endometrial Cells Using Single-Cell RNA-Seq

Emma S Lucas[1,2*], Pavle Vrljicak[1,2*], Maria M Diniz-da-Costa[1,2], Paul J Brighton[2], Chow S Kong[2], Julia Lipecki[3], Katherine Fishwick[2], Joanne Muter[2], Sascha Ott[1,3], and Jan J Brosens[1,2,4]

[1]Tommy's National Centre for Miscarriage Research, University Hospitals Coventry & Warwickshire, Coventry CV2 2DX, UK.

[2]Division of Biomedical Sciences, Clinical Science Research Laboratories, Warwick Medical School, University of Warwick, Coventry CV2 2DX, UK.

[3]Department of Computer Science, University of Warwick, Coventry, CV4 7AL, UK.

[4]Corresponding Author and Lead Contact: Jan Brosens M.D., Ph.D. Clinical Science Research Laboratories, Warwick Medical School, University of Warwick, Coventry CV2 2DX, UK. Tel: +44 2476968704; FAX: +44 2476968653; Email: J.J.Brosens@warwick.ac.uk

*These authors contributed equally.

bioRxiv preprint doi: https://doi.org/10.1101/368829; this version posted July 13, 2018. The copyright holder for this preprint (which was not certified by peer review) is the author/funder. All rights reserved. No reuse allowed without permission.

Summary

The fate of the human endometrium is determined during the mid-luteal window of implantation, coinciding with differentiation of endometrial stromal cells (EnSCs) into specialized decidual cells. In response to successful embryo implantation, differentiating EnSCs transform the endometrium into a decidua that maintains the placenta throughout gestation; whereas falling progesterone levels in the absence of pregnancy lead to tissue destruction and menstrual shedding. We used single-cell RNA sequencing (scRNA-seq) to map the temporal transcriptomic changes in cultured EnSCs along a decidual time-course and in response to withdrawal of differentiation signals. We demonstrate that decidual transformation of EnSCs first involves a continuous and largely synchronous transition through intermediate states before emerging as divergent subpopulations, representing mature decidual cells and stressed cells. Subsequent withdrawal of decidual signals imposes a second branching event, driven primarily by de-differentiation of a subset of cells. Further, scRNA-seq analysis of timed biopsies highlighted endometrial cellular complexity, confirmed the preponderance of different EnSC subpopulations upon progression from mid- to late-luteal phase, and uncovered genes with conserved branching dynamics *in vivo* and *in vitro*. Taken together, our single-cell analysis indicates that multiple EnSC states and dynamic subpopulations of decidual cells underpin endometrial fate decisions during the window of implantation.

Key words: endometrium, decidualization, implantation, single-cell RNA sequencing, transcriptomics, cell state, subpopulation.

bioRxiv preprint doi: https://doi.org/10.1101/368829; this version posted July 13, 2018. The copyright holder for this preprint (which was not certified by peer review) is the author/funder. All rights reserved. No reuse allowed without permission.

Introduction

The human endometrium undergoes iterative cycles of menstrual shedding, regeneration, rapid growth and differentiation in response to the rise and fall in circulating estradiol and progesterone levels (Gellersen and Brosens, 2014). During the mid-luteal phase of the cycle the endometrium begins to remodel intensely, heralding the start of a transient implantation window. This remodeling process is characterized by synchronized transcriptional reprogramming of glandular and luminal epithelium, angiogenesis, influx of uterine natural killer (uNK) and other immune cells, and differentiation of endometrial stromal cells (EnSCs) into secretory decidual cells (Gellersen and Brosens, 2014). Whether or not implantation takes place determines the subsequent fate of the endometrium. In the absence of pregnancy, falling ovarian progesterone levels trigger an inflammatory tissue response resulting in neutrophil infiltration, breakdown of the extracellular matrix, and menstrual shedding (Evans and Salamonsen, 2012, 2014; Jabbour et al., 2006). However, upon implantation, decidualizing EnSCs first encapsulate the conceptus (Weimar et al., 2012; Weimar et al., 2013), and then form a tightly adherent matrix that controls trophoblast invasion and transforms the cycling endometrium into a semi-permanent tissue, which is maintained throughout gestation.

At a molecular level, decidual transformation of EnSCs involves genome-wide remodeling of the chromatin landscape (Vrljicak et al., 2018), wholesale reprogramming of several signaling pathways (Cloke et al., 2008; Leitao et al., 2010), and activation of decidual gene networks (Lynch et al., 2015; Takano et al., 2007). In culture, decidual reprogramming of EnSCs is a multistep process that starts with a burst of free radical production and secretion of inflammatory mediators in response to cyclic adenosine monophosphate (cAMP) and progesterone signaling (Al-Sabbagh et al., 2011; Brighton et al., 2017; Salker et al., 2012). Unlike the secretome produced by undifferentiated EnSCs, decidual inflammation supports blastocyst development in culture and promotes implantation in a mouse model (Peter Durairaj et al., 2017; Salker et al., 2012). After a

bioRxiv preprint doi: https://doi.org/10.1101/368829; this version posted July 13, 2018. The copyright holder for this preprint (which was not certified by peer review) is the author/funder. All rights reserved. No reuse allowed without permission.

lag period of several days, morphologically distinct decidual cells emerge, characterized by nuclear enlargement, abundant cytoplasm and expanded endoplasmic reticulum, reflecting acquisition of a mature secretory phenotype. A hallmark of decidual cells is their resistance to a variety of stress signals that trigger an inflammatory response in undifferentiated EnSCs. Several mechanisms underpin stress resistance of decidual cells, including silencing of c-Jun N-terminal kinase (JNK) and inositol trisphosphate (IP3) signaling (Leitao et al., 2010; Muter et al., 2016), downregulation of O-linked N-acetylglucosamine transferase (OGT), a key enzyme in metabolic stress responses (Muter et al., 2018), and induction of free radical scavengers (Kajihara et al., 2006). Decidualizing EnSCs also highly express *HSD11B1*, coding 11β-hydroxysteroid dehydrogenase type 1. This enzyme catalyzes the conversion of inert cortisone to active cortisol, thus increasing the local levels of anti-inflammatory glucocorticoids at the implantation site (Kuroda et al., 2013). Thus, compared to their fibroblastic progenitor cells, decidual cells are quasi-autonomous, anti-inflammatory and adapted to withstand the intense tissue inflammation caused by deep trophoblast invasion and formation of a hemochorial placenta.

We demonstrated recently that not all EnSCs differentiate into mature decidual cells (Brighton et al., 2017). Instead, a subpopulation of decidualizing EnSCs acquire a senescent phenotype. This subpopulation of stressed decidual cells is then cleared by activated uNK cells through granule exocytosis. We argued that acutely stressed decidual cells may play a pivotal role in kick-starting endometrial remodeling during the implantation window and that their subsequent elimination by uNK cells rejuvenates the endometrium and facilitates its transformation into a gestational tissue (Brighton et al., 2017). In the current study, we employed high-throughput single-cell droplet barcoding to profile individual EnSC transcriptomes across the decidual pathway *in vitro*, to characterize the emerging subpopulations, and to define cellular responses to withdrawal of the differentiation signal. We then extended our scRNA-seq analysis to timed biopsies and

bioRxiv preprint doi: https://doi.org/10.1101/368829; this version posted July 13, 2018. The copyright holder for this preprint (which was not certified by peer review) is the author/funder. All rights reserved. No reuse allowed without permission.

demonstrate that transition of the endometrium from the mid-luteal receptive phase to the late-luteal refractory phase intersects with branching of EnSCs into different subpopulations.

Results and discussion

Single-cell analysis of the decidual pathway in vitro

To construct a temporal transcriptomic map along the decidual pathway, confluent primary EnSCs (passage 2) were treated with 8-bromo-cAMP and MPA (medroxyprogesterone acetate, a progestin) for 8 days followed by withdrawal of the deciduogenic signals for an additional 2 days. Cells were recovered every 48 h and subjected to single-cell analysis using nanoliter droplet barcoding and high throughput sequencing of RNA (Drop-Seq) (Macosko et al., 2015). Approximately 800 cells were captured and sequenced per time-point (Figure S1), with an average of 2,267 unique transcripts per cell, corresponding to an average of 1,282 genes per cell (Figure S2). After initial quality filtering, a total of 4,580 single cells were computationally assigned to 7 transcriptional cell states using a combination of Shared Nearest Neighbour (SNN) and *t*-Distributed Stochastic Neighbor Embedding (*t*-SNE) methods. Figure 1A and 1B show *t*-SNE plots color-coded according to the day of treatment (D0-8) or withdrawal (WD) and transcriptional states (*i*-*vii*), respectively. The expression pattern of the top 10 differential genes in each of the 7 cellular states is presented as a heatmap (Figure 1C and Table S1).

The time-course analysis yielded a number of unexpected observations. First, we identified a discrete population of cells (state *i*) that highly express genes involved in cell cycle progression. This population, confined to undifferentiated (D0) and D2 cultures, were all in G2/M phase of the cell cycle (Figure S3A) and abundantly expressed *ANLN* (Figure 1C), coding the evolutionarily conserved actin binding protein anillin that serves as a key mediator of cytokinesis (Piekny and Maddox, 2010). Immunofluorescence microscopy confirmed the presence of anillin-positive cells in independent EnSC cultures maintained over 4 passages (Figure S3B). A total of 896 genes were

bioRxiv preprint doi: https://doi.org/10.1101/368829; this version posted July 13, 2018. The copyright holder for this preprint (which was not certified by peer review) is the author/funder. All rights reserved. No reuse allowed without permission.

differentially expressed between undifferentiated (state *ii*) and D2 cells (state *iii*) (Table S2), representing the most profound transcriptional change across the decidual pathway, in keeping with the conjecture that decidual initiation is akin to an acute stress response (Al-Sabbagh et al., 2011; Salker et al., 2012). Subsequent progression to state *iv* (D4) involved 289 differentially expressed genes (Table S3). Although heterogeneity in cellular states was observed on D2 and D4, the overall pattern infers a continuum of differentiation-associated gene expression during this initial phase of the decidual process. After 4 days of treatment, however, the temporal pattern in gene expression was lost and cells diverged into two subpopulations, represented by states *v* and *vi* (Figure 1B). We identified 326 differentially expressed genes between these subpopulations of decidual cells (Table S4). Manual mining of the data revealed that state *v* cells highly express genes that confer decidual autonomy (e.g. *DUSP1*, *PLCL1*) and resistance to stress signals (e.g. *HSD11B1*, *IL1RL1*, *GLRX*) (Kuroda et al., 2013; Leitao et al., 2010; Muter et al., 2018; Salker et al., 2016); whereas state *vi* cells are enriched in genes implicated in oxidative apoptosis [e.g. *C10orf10* (also known as decidual protein induced by progesterone, DEPP), *FOXO3*, *NOX4*] and cellular senescence (e.g. *CLU*, *ABI3BP*) (Figure S4) (Guo and Chen, 2015; Kajihara et al., 2006; Latini et al., 2011; Salcher et al., 2017; Trougakos, 2013). The emergence of two transcriptionally distinct cell states after 4 days of differentiation substantiates our recent report demonstrating that primary EnSCs give rise to both mature and senescent decidual subpopulations (Brighton et al., 2017). Withdrawal of the deciduogenic signal for 48 h resulted in the emergence of state *vii* cells, although the response was heterogeneous with multiple cells at this time-point assigned to state *ii* or *vi* (Figure 1B). Compared to either mature (state *v*) or stressed (state *vi*) decidual cells, 341 and 361 genes, respectively, were differentially expressed upon withdrawal of 8-bromo-cAMP and MPA (Tables S5 and S6). Finally, two additional primary cultures from different women were analyzed by scRNA-seq across a partial time-course (D0, D2 and D8) to test the robustness of our findings. Aggregation of data from three biological repeat experiments demonstrated that cells cluster on D0 and D2 by state,

bioRxiv preprint doi: https://doi.org/10.1101/368829; this version posted July 13, 2018. The copyright holder for this preprint (which was not certified by peer review) is the author/funder. All rights reserved. No reuse allowed without permission.

rather than origin of the culture, and confirmed branching of the decidual trajectory into transcriptionally distinct subpopulations by D8 (Figure S5).

Temporal expression and secretion of soluble decidual factors

Sequential changes in the EnSC secretome upon progression through the decidual pathway are thought to underpin various stages of the implantation process, including acquisition of endometrial receptivity in response to release of inflammatory mediators, embryo invasion and activation of uNK cells (Brighton et al., 2017; Garrido-Gomez et al., 2017; Salker et al., 2012). To provide insights into the kinetics of the decidual secretory response, we measured the concentration of different secreted factors in culture supernatant across the decidual time-course and mapped the corresponding transcript levels to individual cells across the 7 cellular states (Figure 2). Prolactin (PRL) and insulin-like growth factor-binding protein 1 (IGFBP1) are widely used decidual markers (Gellersen and Brosens, 2014); and both proteins promote trophoblast invasion (Garrido-Gomez et al., 2017), among other functions. After an initial lag-period, *PRL* and *IGFBP1* transcript levels increased steadily upon decidualization in parallel with protein secretion (Figure 2). Withdrawal of the decidual signal for 48 h attenuated accumulation of both PRL and IGFBP1 in the supernatant. By contrast, expression and secretion of IL-8 was incongruent; with some undifferentiated EnSCs (state *ii*) expressing but not secreting IL-8 whereas the transient rise in IL-8 secretion on D2 (state *iii*) coincided with loss of *IL8* transcripts (Figure 2). This pattern, which also applied to IL-6 (Figure S6), is in keeping with previous observations demonstrating that active release of stored pro-inflammatory mediators plays a role in kick-starting the decidual process (Brighton et al., 2017). Interestingly, a second rise in IL-8 secretion occurred at later time-points, coinciding with the emergence of the two decidual subpopulations, and peaked in response to withdrawal (state *vii*) despite a concurrent fall in mRNA levels. Discordance between expression and secretion was also

bioRxiv preprint doi: https://doi.org/10.1101/368829; this version posted July 13, 2018. The copyright holder for this preprint (which was not certified by peer review) is the author/funder. All rights reserved. No reuse allowed without permission.

apparent for IL-15, a pivotal cytokine for uNK cell activation (Brighton et al., 2017). *IL15* mRNA expression increased markedly during the initial decidual phase but secretion of this cytokine also coincided with emergence of distinct decidual subpopulations after D4. Further, *IL15* transcripts were more abundantly expressed in mature (state *v*) decidual cells when compared to stressed (state *vi*) cells (Figure 2). Taken together, the data show that decidual factors are secreted in a dynamic but temporally restricted manner. Further, the kinetics of these secretory responses are not necessarily aligned to transcriptional activation of corresponding genes.

Co-regulated gene networks

To provide further insight into the genes that drive decidualization (state *ii* to *vi*), 1749 genes with variable expression were used for K-means cluster analysis (Table S7). This analysis yielded 7 co-expressed gene networks, which we ordered in 3 main categories (Figure 3A-C). Category A encompassed 3 gene networks, totaling 867 genes, that were down-regulated during the initial decidual phase (states *iii* & *iv*) and either remained repressed or were re-expressed upon the emergence of the two decidual subpopulations (state *v* and *vi* cells). Gene ontology (GO) analysis revealed that these attenuated networks were significantly enriched in genes involved in translation, mRNA splicing and cell-cell adhesion (Figure 3D and Table S8). Category B, totaling 460 genes, denotes gene networks most highly expressed during either the initial decidual phase (states *iii* and *iv*), whereas category C networks, totaling 421 genes, are prominent in mature (state *v*) and stressed (state *vi*) decidual cells. Notable GO terms enriched in Category B networks included protein folding and cell redox homeostasis. Further, the most notable GO terms in Category C were signal peptide/secretion and type I interferon signaling (Figure 3D).

Cell-fate transitions in decidualizing EnSCs

bioRxiv preprint doi: https://doi.org/10.1101/368829; this version posted July 13, 2018. The copyright holder for this preprint (which was not certified by peer review) is the author/funder. All rights reserved. No reuse allowed without permission.

While aggregation analyses categorize heterogeneous cells in different states or populations, they do so by imposing a discrete framework. Pseudotime measures changes in cell state as a function of progress along a continuous trajectory. We used this approach to reconstruct a decidual pathway with a tree-like structure, reflecting divergence in cell-fate trajectories. However, as the initial transition from undifferentiated cells (states *i* and *ii*) to D2 cells (state *iii*) represents a precipitous transcriptional change, we restricted pseudotime modelling to cells under continuous decidual stimulation (D2-D8) and in response to withdrawal of 8-bromo-cAMP and MPA. Two branching events were identified along the decidual pathway (Figure 4A), subdividing the trajectory into multiple segments populated by 5 clusters of cells, labelled 1-5 (Figure 4B). Cluster 1 primarily constituted cells expressing a continuum of differentiation genes between D2 to D4. Branch point 1 signaled cell fate divergence into pathway leading to stressed/senescent decidual cells (cluster 3) and mature decidual cells (cluster 2). The top 50 branch-dependent genes are depicted in a modified heatmap, clustered hierarchically to visualize modules of genes that have similar lineage-dependent expression patterns (Figure 4C). Among the most prominent upregulated genes in cluster 2 cells are several that encode for secreted senescence-associated factors, including *CLU* (clusterin or apoliprotein J), *ABI3BP* [ABI family member 3 binding protein, also known as target of NESH-SH3 (TARSH)], and *IGFBP1* (Diep et al., 2016; Latini et al., 2011; Trougakos, 2013). By contrast, senescent decidual cells downregulated *CXCL14* whereas the expression of this chemokine involved uNK cell chemotaxis was maintained in mature decidual cells (Mokhtar et al., 2010). *FTL*, *SCARA5* and *PGRMC2*, along with known decidual genes such as *GLRX* and *IL1RL1*, were part of a prominent module of co-regulated genes selectively enhanced in mature decidual cells (Figure 4C). *FTL* encodes for ferritin light chain (L-ferritin) and *SCARA5* (scavenger receptor class A member 5) for the L-ferritin receptor (Mendes-Jorge et al., 2014), suggesting that iron uptake, storage and detoxification are important for decidual function. *PGRMC2* encodes progesterone receptor membrane component 2. Although the precise function of this putative progesterone

bioRxiv preprint doi: https://doi.org/10.1101/368829; this version posted July 13, 2018. The copyright holder for this preprint (which was not certified by peer review) is the author/funder. All rights reserved. No reuse allowed without permission.

binding protein is not known, deletion of *Pgrmc2* in mice leads to post-implantation embryonic demise, suggestive of a decidual defect, and accelerated endometrial senescence (Clark et al., 2017).

Withdrawal of differentiation signals on D8 of the decidual time-course triggered further cell-fate divergence (branch point 2) and the emergence of cluster 4 and 5 cells (Figure 4B). Modeling of gene dynamics at this branching point revealed that cluster 4 cells upregulate numerous genes that are prominently expressed in undifferentiated EnSCs (state ii), indicating de-differentiation of a subpopulation of decidual cells (Figure S7).

Secreted markers of decidual subpopulations

Modeling of gene dynamics at branch point 1 in the decidual pathway suggested that both mature and senescent decidual cells contribute to the peri-implantation secretome. We postulated that secretion of clusterin, a stress-induced molecular chaperone molecule, could serve as a selective marker for senescent decidual cells (state vi), whereas IL15 and CXCL14 secretion is likely restricted to the mature subpopulation (state v). We first employed MAGIC (Markov Affinity-based Graph Imputation of Cells) to impute missing values in our data and then established the gene-gene relationship between *CLU*, *IL15*, and *CXCL14* in decidualizing cells. As shown in Figure 5A, high *CLU* and high *IL15* or *CXCL14* expression were mutually exclusive in decidualizing EnSCs. To test our hypothesis further, three independent primary EnSC cultures were first treated with 8-bromo-cAMP and MPA for 6 days and then co-cultured with or without uNK cells isolated from luteal phase endometrial biopsies. uNK cells selectively target senescent decidual cells, perforate their membrane with perforin, and then trigger apoptosis by releasing granzyme into the cytoplasm. Analysis of culture supernatant revealed that uNK cells do not impact on decidual IL15 secretion. As anticipated, secreted clusterin levels started to rise sharply on D6 of

bioRxiv preprint doi: https://doi.org/10.1101/368829; this version posted July 13, 2018. The copyright holder for this preprint (which was not certified by peer review) is the author/funder. All rights reserved. No reuse allowed without permission.

the time-course; and this response was markedly blunted upon co-culture with uNK cells ($P < 0.01$). Interestingly, although secreted CXCL14 levels plateaued around D6, uNK cell-mediated clearance of senescent decidual cells further enhanced secretion of this chemokine ($P < 0.05$). Taken together, the data suggest that the decidual microenvironment is determined by the relative abundance of, and crosstalk between, decidual subpopulations; and further dynamically modified by uNK cells.

Single-cell analysis of timed endometrial biopsies

Based on the single-cell analysis in culture, we postulated that dynamic progression of EnSCs along an equivalent cell-state trajectory underpins the transition of endometrium from a receptive to a refractory state. To test this hypothesis, freshly isolated cells from seven endometrial biopsies were subjected to scRNA-seq. The biopsies were timed relatively to the pre-ovulatory luteinizing hormone (LH) surge to coincide with the mid-luteal implantation window (LH+8; n=3) or the start of the refractory late-luteal phase (LH+10; n=4). Out of a total of 4,797 cells, 3,304 passed our quality filtering with an average of 2,774 unique transcripts per cell, corresponding to an average of 1,284 genes per cell. The cells were computationally separated into stromal (n=2,373), epithelial (n=386), endothelial (n=159), and immune cells (n=386). The relative underrepresentation of epithelial cells is accounted for by the resistance of the glands to mild enzymatic digestion used to isolate single cells from the stromal fraction of the biopsies. The expression pattern of the top 10 marker genes for each of the four major cell populations in the endometrium is depicted as a heatmap (Figure S8A). Figures 6A and 6B show *t*-SNE plots color-coded according to cell population and the relative contribution of different biopsy samples to each population, respectively. As was the case for primary cultures, we identified a discrete, highly proliferative (HP) subpopulation of EnSCs, representing 1.3% of all stromal cells. Next, we performed

bioRxiv preprint doi: https://doi.org/10.1101/368829; this version posted July 13, 2018. The copyright holder for this preprint (which was not certified by peer review) is the author/funder. All rights reserved. No reuse allowed without permission.

pseudotime analysis to test our hypothesis that transition of endometrium from a receptive to a refractory state coincides with progression of EnSCs along a cell-state trajectory. In addition to two minor branch points (designated 1 and 2) (Figure S8B and S8C), pseudotime analysis yielded one major branch point (designated 3) as highlighted in Figure 6C. The top 50 dynamic genes at this major *in vivo* branch point are depicted in a modified heatmap (Figure S8D). Strikingly, the timing of the biopsy relative to the LH surge mapped closely to the progress of EnSCs along the cell-fate trajectory in all but one sample. This sample, designated P1, was obtained at LH+10 but aligned in pseudotime closer to LH+8 samples, indicating that the biopsy was likely mistimed.

We speculated that the relationship between genes that drive branching of cellular trajectories to alternative cell fates would, at least partly, be conserved *in vivo* and *in vitro*. To test this hypothesis, we selected the top 50 genes that distinguished branch point 1 in the decidual time-course (Figure 4C) and calculated the Pearson correlations for each gene pair across stromal cells in the biopsy data (Figure 6D, left panel). We added those to correlation coefficients in the *in vitro* data generating a sum of coefficients ranging from 2, for positively correlated, to -2, for negatively correlated gene pairs. The reversed analysis was also carried out by calculating the conservation in the *in vitro* data of the top 50 gene-gene interactions that drive divergence of EnSCs at the major *in vivo* branch point (Figure 6D, right panel). Congruency was defined as the sum of correlation coefficients of >1 or <-1 for positively and negatively co-regulated genes, respectively. Using this criterion, 27% of the top 50 gene pairs in the *in vitro* data (branch point 1) were congruent with the *in vivo* analysis whereas 19% of the top 50 gene pairs in the *in vivo* data (branch point 3) conformed to the *in vitro* data. For example, gene pairs that mark the divergence of differentiating EnSC into mature (e.g. *SCARA5*, *IL1RL1*, and *GLRX*) and senescent (e.g. *ABI3BP*, *CLU* and *IGFBP1*) subpopulations were maintained *in vivo*. Other gene-gene interactions were less conserved. For instance, *SCARA5* and *PGRMC2* are co-regulated *in vitro* but this association was not maintained in EnSCs *in vivo*. Hypergeometric testing revealed that genes involved in branching

bioRxiv preprint doi: https://doi.org/10.1101/368829; this version posted July 13, 2018. The copyright holder for this preprint (which was not certified by peer review) is the author/funder. All rights reserved. No reuse allowed without permission.

dynamics *in vitro* (branch point 1) and *in vivo* (branch point 3) are significantly more co-regulated than expected by chance alone ($P < 10^{-82}$ and $P < 10^{-33}$, respectively; Figure S9). Taken together, the data show that multiple genes involved in the segregation of differentiating EnSCs into mature and stressed subpopulations in culture are also implicated in endometrial fate decisions during the window of implantation.

Materials and Methods

Ethical approval and sample collection. The study was approved by the NHS National Research Ethics-Hammersmith and Queen Charlotte's & Chelsea Research Ethics Committee (1997/5065). Endometrial biopsies were obtained from women attending the Implantation Clinic, a dedicated research clinic at University Hospitals Coventry and Warwickshire (UHCW) National Health Service Trust. Timed endometrial biopsies, relative to the preovulatory LH surge, were obtained using a Wallach Endocell endometrial sampler with written informed consent in accordance with The Declaration of Helsinki (2000) guidelines.

Primary endometrial stromal cell (EnSC) culture. Endometrial biopsies were collected in DMEM-F12 media supplemented with 10 % dextran coated charcoal-stripped FBS (DCC) and processed for primary EnSC culture as described (Barros et al., 2016). For decidualization studies, confluent monolayers of human endometrial stromal cells (EnSCs) were incubated overnight at 37 °C with 5 % CO2 in phenol red-free DMEM/F-12 containing 2 % DCC, containing antibiotic/antimycotic and L-glutamine (2 % media). To induce differentiation, cells were treated in 2 % DCC with 0.5 mM 8-bromo-cAMP (Sigma-Aldrich, Poole, UK) and 1 μM medroxyprogesterone acetate (MPA; Sigma-Aldrich, UK) for the indicated time-points.

Droplet generation and single cell sequencing (Drop-seq). Single cell transcriptomes were captured in aqueous droplets containing barcoded beads using a microfluidic system (scRNAseq: Dolomite Bio, Royston, UK) according to the manufacturer's protocol and based on the Drop-seq

bioRxiv preprint doi: https://doi.org/10.1101/368829; this version posted July 13, 2018. The copyright holder for this preprint (which was not certified by peer review) is the author/funder. All rights reserved. No reuse allowed without permission.

method described by Macosko and colleagues (Macosko et al., 2015). Briefly, cells in suspension were placed into the remote chamber of the scRNAseq system. Barcoded beads in lysis buffer at a concentration of 280 beads/ µl were loaded into the sample loop. Cell and bead solutions were run at a flow rate of 30 µl/ min into a fluorophilic glass microfluidic chip with 100 µm etch depth (Single Cell RNA-seq Chip, Dolomite Bio, Cambridge, UK) with droplet generation oil (Bio-Rad Laboratories, UK) at a flow rate of 200 µl/ min for 15-18 minutes. Droplets were collected into a 50 ml Falcon tube, quality checked using a C-Chip Fuchs-Rosenthal Haemocytometer (Labtech, Heathfield, UK) and bead doublets counted. Droplet breakage, bead isolation and reverse transcription were performed exactly as described by Macosko and Goldman (Drop-Seq Laboratory Protocol version 3.1, www.mccarrolllab.com/dropseq). All beads from a single run were processed in one batch through Exonuclease I digestion. PCR was performed on 8000 beads per reaction, with two reactions per sample, to give ~800 single-cell transcriptomes attached to microparticles (STAMPS) per timepoint. PCR conditions were as per Macosko and Goldman. Ampure XP clean-up was performed according to standard Illumina RNAseq protocols with a 0.6X beads to sample ratio. cDNA was eluted in 12 µl and quality and size assessed using an Agilent Bioanalyzer High Sensitivity DNA chip. For tagmentation 600 pg cDNA, as determined by Qubit High Sensitivity DNA assay, was processed according to Macosko and Goldman using Illumina Nextera XT DNA Sample Kit and Indexing Kit. Tagmented libraries were cleaned up using AMPure XP beads as before, with a 0.6× beads ratio followed by a repeat clean-up using 1× beads. Eluted libraries were analysed using Agilent Bioanalyzer High Sensitivity DNA chip to assess quality and determine library size and concentration was determined by Qubit High Sensitivity DNA assay. Library dilution and denaturation was performed as per standard Illumina protocols and sequenced using NextSeq High Output 75 cycle V2 kit.

Drop-seq data alignment and quantification. Initial Drop-seq (Macosko et al., 2015) data processing was performed using Drop-seq_tools-1.0.1 following the protocol described by Nemesh

bioRxiv preprint doi: https://doi.org/10.1101/368829; this version posted July 13, 2018. The copyright holder for this preprint (which was not certified by peer review) is the author/funder. All rights reserved. No reuse allowed without permission.

(seqAlignmentCookbook_v1.2Jan2016.pdf, http://mccarrolllab.com/dropseq). Briefly, reads with low-quality bases in either cell or molecular barcode were filtered and trimmed for contaminating primer or poly-A sequence. Sequencing errors in barcodes were inferred and corrected, as implemented by Drop-seq_tools-1.0.1. Reads were aligned to the hg19 (Human) reference genome concatenated with ERCC annotations using STAR-2.5.3a (Dobin et al., 2013), with the Gencode21 (Human) as reference transcriptome. Uniquely mapped reads, with ≤ 1 insertion or deletion, were used in quantification. Finally, the DigitalExpression tool (Macosko et al., 2015) was used to obtain the digital gene expression (DGE) matrix for each sample. Cell numbers were selected computationally from the inflection point in a cumulative distribution of reads plotted against the cell barcodes ordered by descending number of reads (Figure S1). Cell barcodes beyond the inflection point are believed to represent 'ambient RNA' (e.g. contaminating RNA from damaged cells), not cellular transcriptomes, and therefore excluded from further analysis. This resulted in ~800 cells per time-point, matching the number anticipated from processed bead counts.

Cell aggregation analysis. Analysis of DGE data was performed with Seurat v2 (Satija et al., 2015). To select high quality data for analysis, cells were included when at least 200 genes were detected, while genes were included if they were detected in at least 3 cells. Cells which had more than 4500 genes were excluded from the analysis as were cells with more than 5% mitochondrial gene transcripts to minimize doublets and low-quality (broken or damaged) cells, respectively. After scaling and normalization of the raw counts in the DGE matrix, cell-cycle regression was applied. For cell aggregation, a set of highly variable genes was first identified, with an average expression mean between 0.0125 and 3 and a Log Variant to Mean Ratio of at least 0.5, which were used to perform principal component (PC) analysis. Judged by their statistical significance and the robustness of the results, the first 10 PCs were subsequently used as inputs for clustering via shared nearest neighbour (SNN) and subsequent *t*-distributed stochastic neighbour embedding (*t*-SNE) representation. The Seurat function 'FindAllMarkers' employing the Wilcox test was used

bioRxiv preprint doi: https://doi.org/10.1101/368829; this version posted July 13, 2018. The copyright holder for this preprint (which was not certified by peer review) is the author/funder. All rights reserved. No reuse allowed without permission.

to identify marker genes for each cell state cluster in the *t*-SNE representation. To obtain independent estimation of the number of unique cell-types we used SC3 v1.3.18 (Kiselev et al., 2017), applying a consensus strategy (Figure S10) and Tracy-Widom theory on random matrices to estimate the optimal number of clusters (k).

Co-regulated gene networks. K-means cluster analysis was performed in MeV v4.8 (Saeed et al., 2003) to group marker genes based on co-expression across cell state clusters. Fig. of Merit (FoM) was run first to determine the number of expression patterns (k). The predictive power of the k-means algorithm was estimated using a Fig. of merit (FOM) values for k from 1 to 20. K-means clustering was run using Pearson correlation metric for a maximum of 50 iterations. Gene ontology analysis was performed on the clustered genes using DAVID (Huang da et al., 2009).

Trajectory analysis. Trajectory analysis was performed with Monocle v2.6.1 (Trapnell et al., 2014) (Qiu et al., 2017a; Qiu et al., 2017b). Branch-point genes were identified with Branched Expression Analysis Modeling (BEAM) function.

Gene expression correlation. To test gene expression correlation between pairs of genes, expression was imputed for every cells using Markov Affinity-based Graph Imputation of Cells (MAGIC) (van Dijk et al., 2017). Pearson correlation coefficients were calculated for top 50 genes determining the different trajectories at informative branch-points. To assess congruency between the time-course and biopsy datasets, the correlation coefficients were added resulting in sum of coefficients between -2 and +2.

Uterine natural killer (uNK) cell isolation. Supernatant from freshly digested EnSC cultures was collected and red blood cells excluded through Ficoll-Paque density gradient centrifugation. uNK cells were isolated by magnetic activated cell separation (MACS; Miltenyi Biotec, Bergisch Gladbach, Germany) using phycoerythrin (PE)-conjugated anti-CD56 antibody (Bio-Legend, San

bioRxiv preprint doi: https://doi.org/10.1101/368829; this version posted July 13, 2018. The copyright holder for this preprint (which was not certified by peer review) is the author/funder. All rights reserved. No reuse allowed without permission.

Diego, CA, USA), as per manufacturer's instructions. The $CD56^+$ positive fraction was collected by centrifugation and cultured in suspension for up to 5 days in RPMI media (Sigma-Aldrich) supplemented with 10% DCC-FBS, 1× Antibiotic-Antimycotic, and 2 ng/ml IL-15 (Sigma-Aldrich) to aid uNK cell maturation. To increase yield, uNK harvests from 3-5 patients were pooled. For co-culture experiments, uNK cells were pelleted and re-suspended in 2% DMEM/F12 without IL-15 and co-cultured with EnSC monolayers at day 6 of 8-bromo cAMP and MPA treatment. Supernatant was collected every 2 days and centrifuged to clear cell debris prior to storage at -20°C.

Enzyme-linked immunosorbent assay (ELISA). Cultured EnSCs from individual patients were seeded at identical densities and treated in accordance with experimental schedules. Analytes in collected supernatant were analysed by ELISAs exactly as per manufacturer's instructions (DuoSet ELISA kits, Bio-Techne, Abingdon, UK). Standard curves were fitted to a 4-parameter logistic fit curve in GraphPad Prism software and sample concentrations interpolated from these graphs.

Immunofluorescence Microscopy. Confluent EnSC monolayers in 24-well plates were fixed in 4% paraformaldehyde, permeabilized in 0.5% Titon-X100 and blocked with 1% BSA/PBS. Cells were probed overnight at 4°C with antibodies targeting anillin (mouse monoclonal anti-ANLN antibody (Sigma-Aldrich) diluted 1:75 in 0.1%BSA/PBS). Labelled cells were stained with Alexa-Fluor™ 594 anti-mouse secondary antibody and counterstained with a ProLong® Gold Antifade DAPI Mounting media. Imaging was achieved on an EVOS FL fluorescent microscope (ThermoFisher Scientific). The number of anillin positive cells in 3 random images was counted as a percentage of total (DAPI stained) cells.

bioRxiv preprint doi: https://doi.org/10.1101/368829; this version posted July 13, 2018. The copyright holder for this preprint (which was not certified by peer review) is the author/funder. All rights reserved. No reuse allowed without permission.

References

Al-Sabbagh, M., Fusi, L., Higham, J., Lee, Y., Lei, K., Hanyaloglu, A.C., Lam, E.W., Christian, M., and Brosens, J.J. (2011). NADPH oxidase-derived reactive oxygen species mediate decidualization of human endometrial stromal cells in response to cyclic AMP signaling. Endocrinology *152*, 730-740.

Barros, F.S.V., Brosens, J.J., and Brighton, P.J. (2016). Isolation and Primary Culture of Various Cell Types from Whole Human Endometrial Biopsies. bio-protocol *6*.

Brighton, P.J., Maruyama, Y., Fishwick, K., Vrljicak, P., Tewary, S., Fujihara, R., Muter, J., Lucas, E.S., Yamada, T., Woods, L., *et al.* (2017). Clearance of senescent decidual cells by uterine natural killer cells in cycling human endometrium. Elife *6*.

Clark, N.C., Pru, C.A., Yee, S.P., Lydon, J.P., Peluso, J.J., and Pru, J.K. (2017). Conditional Ablation of Progesterone Receptor Membrane Component 2 Causes Female Premature Reproductive Senescence. Endocrinology *158*, 640-651.

Cloke, B., Huhtinen, K., Fusi, L., Kajihara, T., Yliheikkila, M., Ho, K.K., Teklenburg, G., Lavery, S., Jones, M.C., Trew, G., *et al.* (2008). The androgen and progesterone receptors regulate distinct gene networks and cellular functions in decidualizing endometrium. Endocrinology *149*, 4462-4474.

Diep, C.H., Knutson, T.P., and Lange, C.A. (2016). Active FOXO1 Is a Key Determinant of Isoform-Specific Progesterone Receptor Transactivation and Senescence Programming. Mol Cancer Res *14*, 141-162.

Dobin, A., Davis, C.A., Schlesinger, F., Drenkow, J., Zaleski, C., Jha, S., Batut, P., Chaisson, M., and Gingeras, T.R. (2013). STAR: ultrafast universal RNA-seq aligner. Bioinformatics (Oxford, England) *29*, 15-21.

Evans, J., and Salamonsen, L.A. (2012). Inflammation, leukocytes and menstruation. Rev Endocr Metab Disord *13*, 277-288.

bioRxiv preprint doi: https://doi.org/10.1101/368829; this version posted July 13, 2018. The copyright holder for this preprint (which was not certified by peer review) is the author/funder. All rights reserved. No reuse allowed without permission.

Evans, J., and Salamonsen, L.A. (2014). Decidualized human endometrial stromal cells are sensors of hormone withdrawal in the menstrual inflammatory cascade. Biol Reprod *90*, 14.

Garrido-Gomez, T., Dominguez, F., Quinonero, A., Diaz-Gimeno, P., Kapidzic, M., Gormley, M., Ona, K., Padilla-Iserte, P., McMaster, M., Genbacev, O., *et al.* (2017). Defective decidualization during and after severe preeclampsia reveals a possible maternal contribution to the etiology. Proc Natl Acad Sci U S A *114*, E8468-E8477.

Gellersen, B., and Brosens, J.J. (2014). Cyclic decidualization of the human endometrium in reproductive health and failure. Endocr Rev *35*, 851-905.

Guo, S., and Chen, X. (2015). The human Nox4: gene, structure, physiological function and pathological significance. J Drug Target *23*, 888-896.

Huang da, W., Sherman, B.T., and Lempicki, R.A. (2009). Systematic and integrative analysis of large gene lists using DAVID bioinformatics resources. Nature protocols *4*, 44-57.

Jabbour, H.N., Kelly, R.W., Fraser, H.M., and Critchley, H.O. (2006). Endocrine regulation of menstruation. Endocr Rev *27*, 17-46.

Kajihara, T., Jones, M., Fusi, L., Takano, M., Feroze-Zaidi, F., Pirianov, G., Mehmet, H., Ishihara, O., Higham, J.M., Lam, E.W., *et al.* (2006). Differential expression of FOXO1 and FOXO3a confers resistance to oxidative cell death upon endometrial decidualization. Mol Endocrinol *20*, 2444-2455.

Kiselev, V.Y., Kirschner, K., Schaub, M.T., Andrews, T., Yiu, A., Chandra, T., Natarajan, K.N., Reik, W., Barahona, M., Green, A.R., *et al.* (2017). SC3: consensus clustering of single-cell RNA-seq data. Nature methods *14*, 483-486.

Kuroda, K., Venkatakrishnan, R., Salker, M.S., Lucas, E.S., Shaheen, F., Kuroda, M., Blanks, A., Christian, M., Quenby, S., and Brosens, J.J. (2013). Induction of 11beta-HSD 1 and activation of distinct mineralocorticoid receptor- and glucocorticoid receptor-dependent gene networks in decidualizing human endometrial stromal cells. Mol Endocrinol *27*, 192-202.

bioRxiv preprint doi: https://doi.org/10.1101/368829; this version posted July 13, 2018. The copyright holder for this preprint (which was not certified by peer review) is the author/funder. All rights reserved. No reuse allowed without permission.

Latini, F.R., Hemerly, J.P., Freitas, B.C., Oler, G., Riggins, G.J., and Cerutti, J.M. (2011). ABI3 ectopic expression reduces in vitro and in vivo cell growth properties while inducing senescence. BMC Cancer *11*, 11.

Leitao, B., Jones, M.C., Fusi, L., Higham, J., Lee, Y., Takano, M., Goto, T., Christian, M., Lam, E.W., and Brosens, J.J. (2010). Silencing of the JNK pathway maintains progesterone receptor activity in decidualizing human endometrial stromal cells exposed to oxidative stress signals. FASEB J *24*, 1541-1551.

Lynch, V.J., Nnamani, M.C., Kapusta, A., Brayer, K., Plaza, S.L., Mazur, E.C., Emera, D., Sheikh, S.Z., Grutzner, F., Bauersachs, S., *et al.* (2015). Ancient transposable elements transformed the uterine regulatory landscape and transcriptome during the evolution of mammalian pregnancy. Cell Rep *10*, 551-561.

Macosko, E.Z., Basu, A., Satija, R., Nemesh, J., Shekhar, K., Goldman, M., Tirosh, I., Bialas, A.R., Kamitaki, N., Martersteck, E.M., *et al.* (2015). Highly Parallel Genome-wide Expression Profiling of Individual Cells Using Nanoliter Droplets. Cell *161*, 1202-1214.

Mendes-Jorge, L., Ramos, D., Valenca, A., Lopez-Luppo, M., Pires, V.M., Catita, J., Nacher, V., Navarro, M., Carretero, A., Rodriguez-Baeza, A., *et al.* (2014). L-ferritin binding to scara5: a new iron traffic pathway potentially implicated in retinopathy. PLoS One *9*, e106974.

Mokhtar, N.M., Cheng, C.W., Cook, E., Bielby, H., Smith, S.K., and Charnock-Jones, D.S. (2010). Progestin regulates chemokine (C-X-C motif) ligand 14 transcript level in human endometrium. Mol Hum Reprod *16*, 170-177.

Muter, J., Alam, M.T., Vrljicak, P., Barros, F.S.V., Ruane, P.T., Ewington, L.J., Aplin, J.D., Westwood, M., and Brosens, J.J. (2018). The Glycosyltransferase EOGT Regulates Adropin Expression in Decidualizing Human Endometrium. Endocrinology *159*, 994-1004.

Muter, J., Brighton, P.J., Lucas, E.S., Lacey, L., Shmygol, A., Quenby, S., Blanks, A.M., and Brosens, J.J. (2016). Progesterone-Dependent Induction of Phospholipase C-Related Catalytically

bioRxiv preprint doi: https://doi.org/10.1101/368829; this version posted July 13, 2018. The copyright holder for this preprint (which was not certified by peer review) is the author/funder. All rights reserved. No reuse allowed without permission.

Inactive Protein 1 (PRIP-1) in Decidualizing Human Endometrial Stromal Cells. Endocrinology *157*, 2883-2893.

Peter Durairaj, R.R., Aberkane, A., Polanski, L., Maruyama, Y., Baumgarten, M., Lucas, E.S., Quenby, S., Chan, J.K.Y., Raine-Fenning, N., Brosens, J.J., *et al.* (2017). Deregulation of the endometrial stromal cell secretome precedes embryo implantation failure. Mol Hum Reprod *23*, 582.

Piekny, A.J., and Maddox, A.S. (2010). The myriad roles of Anillin during cytokinesis. Semin Cell Dev Biol *21*, 881-891.

Qiu, X., Hill, A., Packer, J., Lin, D., Ma, Y.A., and Trapnell, C. (2017a). Single-cell mRNA quantification and differential analysis with Census. Nature methods *14*, 309-315.

Qiu, X., Mao, Q., Tang, Y., Wang, L., Chawla, R., Pliner, H.A., and Trapnell, C. (2017b). Reversed graph embedding resolves complex single-cell trajectories. Nature methods *14*, 979-982.

Saeed, A.I., Sharov, V., White, J., Li, J., Liang, W., Bhagabati, N., Braisted, J., Klapa, M., Currier, T., Thiagarajan, M., *et al.* (2003). TM4: a free, open-source system for microarray data management and analysis. BioTechniques *34*, 374-378.

Salcher, S., Hermann, M., Kiechl-Kohlendorfer, U., Ausserlechner, M.J., and Obexer, P. (2017). C10ORF10/DEPP-mediated ROS accumulation is a critical modulator of FOXO3-induced autophagy. Mol Cancer *16*, 95.

Salker, M.S., Hosseinzadeh, Z., Alowayed, N., Zeng, N., Umbach, A.T., Webster, Z., Singh, Y., Brosens, J.J., and Lang, F. (2016). LEFTYA Activates the Epithelial Na+ Channel (ENaC) in Endometrial Cells via Serum and Glucocorticoid Inducible Kinase SGK1. Cell Physiol Biochem *39*, 1295-1306.

Salker, M.S., Nautiyal, J., Steel, J.H., Webster, Z., Sucurovic, S., Nicou, M., Singh, Y., Lucas, E.S., Murakami, K., Chan, Y.W., *et al.* (2012). Disordered IL-33/ST2 activation in decidualizing stromal cells prolongs uterine receptivity in women with recurrent pregnancy loss. PLoS One *7*, e52252.

bioRxiv preprint doi: https://doi.org/10.1101/368829; this version posted July 13, 2018. The copyright holder for this preprint (which was not certified by peer review) is the author/funder. All rights reserved. No reuse allowed without permission.

Satija, R., Farrell, J.A., Gennert, D., Schier, A.F., and Regev, A. (2015). Spatial reconstruction of single-cell gene expression data. Nature biotechnology *33*, 495-502.

Takano, M., Lu, Z., Goto, T., Fusi, L., Higham, J., Francis, J., Withey, A., Hardt, J., Cloke, B., Stavropoulou, A.V., *et al.* (2007). Transcriptional cross talk between the forkhead transcription factor forkhead box O1A and the progesterone receptor coordinates cell cycle regulation and differentiation in human endometrial stromal cells. Mol Endocrinol *21*, 2334-2349.

Trapnell, C., Cacchiarelli, D., Grimsby, J., Pokharel, P., Li, S., Morse, M., Lennon, N.J., Livak, K.J., Mikkelsen, T.S., and Rinn, J.L. (2014). The dynamics and regulators of cell fate decisions are revealed by pseudotemporal ordering of single cells. Nature biotechnology *32*, 381-386.

Trougakos, I.P. (2013). The molecular chaperone apolipoprotein J/clusterin as a sensor of oxidative stress: implications in therapeutic approaches - a mini-review. Gerontology *59*, 514-523.

van Dijk, D., Nainys, J., Sharma, R., Kathail, P., Carr, A.J., Moon, K.R., Mazutis, L., Wolf, G., Krishnaswamy, S., Pe, *et al.* (2017). MAGIC: A diffusion-based imputation method reveals gene-gene interactions in single-cell RNA-sequencing data. bioRxiv.

Vrljicak, P., Lucas, E.S., Lansdowne, L., Lucciola, R., Muter, J., Dyer, N.P., Brosens, J.J., and Ott, S. (2018). Analysis of chromatin accessibility in decidualizing human endometrial stromal cells. FASEB J, fj201701098R.

Weimar, C.H., Kavelaars, A., Brosens, J.J., Gellersen, B., de Vreeden-Elbertse, J.M., Heijnen, C.J., and Macklon, N.S. (2012). Endometrial stromal cells of women with recurrent miscarriage fail to discriminate between high- and low-quality human embryos. PLoS One *7*, e41424.

Weimar, C.H., Macklon, N.S., Post Uiterweer, E.D., Brosens, J.J., and Gellersen, B. (2013). The motile and invasive capacity of human endometrial stromal cells: implications for normal and impaired reproductive function. Hum Reprod Update *19*, 542-557.

bioRxiv preprint doi: https://doi.org/10.1101/368829; this version posted July 13, 2018. The copyright holder for this preprint (which was not certified by peer review) is the author/funder. All rights reserved. No reuse allowed without permission.

Figure legends

Figure 1. **Single-cell RNA sequencing of decidualizing EnSCs reveals progression through distinct transcriptional states and emergence of two subpopulations.** (**A**) *t*-SNE projection of 4,580 EnSCs, color-coded according to the duration (days) of treatment with 8-bromo-cAMP and MPA. (**B**) The same *t*-SNE plot but now color-coded according cell state (*i-vii*). (**C**) Heatmap of the top 10 marker genes for each of the 7 cell states. Each column represents one of 4,580 EnSCs. Expression for each gene is scaled (*z*-scored) across cells. Yellow, purple and black represents high, low or undetectable expression of a given marker gene, respectively.

Figure 2. **Comparative analysis of expression and secretion of decidual markers and cytokines.** (**A**) The expression of decidual marker genes (*PRL* and *IGFBP1*) and cytokines (*IL8* and *IL15*) was overlaid on the *t*-SNE plot. Cells expressing specific genes are colored blue with color intensity reflecting the level of expression. (**B**) Violin plots showing relative levels of expression for the same genes across the cell state clusters. (**C**) Comparison of the temporal pattern of expression versus secretion of PRL, IGFBP1, IL-8, and IL-15. The level of secretion was determined by ELISA of culture supernatant at the indicated time-point.

Figure 3. **K-means cluster analysis of co-regulated gene networks**. Genes with variable expression levels between cell state clusters were grouped according to co-expression groups A1-3 (A1 – 422 genes; A2 – 297 genes; A3 – 148 genes), B1-2 (B1- 221 genes; B2 – 239 genes) and C1-2 (C1 – 226 genes; C2 – 195 genes) using k-means clustering (k=7). (**A-C**) Line graphs represent the average normalized gene expression in each cell-type (y-axis) for each of the cell state clusters (x-axis). (**D**) Top enriched Gene Ontology categories in each co-expressed group. Benjamini adjusted p-values shown on the x-axis.

Figure 4. **Construction of the decidualization trajectory by pseudotime analysis**. (**A**) Using Monocle, cells were ordered along a trajectory of differentiation, or pseudotime. (**B**) Two

bioRxiv preprint doi: https://doi.org/10.1101/368829; this version posted July 13, 2018. The copyright holder for this preprint (which was not certified by peer review) is the author/funder. All rights reserved. No reuse allowed without permission.

branching events along the decidual pathway subdivide the trajectory into 5 cell clusters, representing different transitional states and alternative cell fates. (**C**) Heatmap shows gene dynamics during cell state transition at branch point 1. Columns are points in pseudotime while rows represent the 50 most dynamic genes at the branch point. The beginning of pseudotime is in the middle of the heatmap and the trajectory towards mature and senescent cells are depicted on the left and right, respectively. Hierarchical clustering visualizes modules of genes with similar lineage-dependent expression patterns.

Figure 5. **uNK cells modify the decidual microenvironment by targeting stressed (state vi) cells.** (**A**) Scatter plot showing the 2D relationship of the indicated gene pairs in mature (state v) and stressed (state vi) decidual cells after MAGIC. (**B**) Four independent primary EnSC cultures were decidualized with 8-bromo-cAMP and MPA (C+M) for the indicated days. The culture medium was refreshed every 48 h and the concentration of clusterin, IL-15, and CXCL14 determined in spent medium measured by ELISA. On day 6 of decidualization, 5,000 primary uNK cells per well were added to confluent decidual cells cultured in 6-well plates. The data show mean plus standard deviation of 4 independent experiments. ** indicate $P < 0.01$ and * $P < 0.05$.

Figure 6. **Mapping of EnSC trajectory across the window of implantation *in vivo***. (**A**) *t*-SNE plot of 3,304 cells isolated from 7 LH-timed biopsies captures all major endometrial cell types, including epithelial cells (EpC), immune cells (IC), endothelial cells (IC), stromal cells (EnSC) and a discrete but transcriptionally distinct highly proliferative (HP) stromal subpopulation. (**B**) *t*-SNE plot color-coded to indicate the contribution of each biopsy (designated P1-7) to each endometrial cell type. (**C**) Construction of the EnSC trajectory by pseudotime analysis upon progression of the endometrium from the mid-luteal receptive phase (LH+8) to the late-luteal post-receptive phase (LH+10) of the menstrual cycle. Using Monocle, cells were ordered along a trajectory of differentiation, characterized by a major branching point. (**D**) Heatmap depicting the sum of correlation coefficients of the top 50 gene-gene interactions at *in vitro* branch point 1 (i.e.

bioRxiv preprint doi: https://doi.org/10.1101/368829; this version posted July 13, 2018. The copyright holder for this preprint (which was not certified by peer review) is the author/funder. All rights reserved. No reuse allowed without permission.

divergence of decidualizing EnSC into mature and stressed/senescent subpopulations) and at the major branch point in the in vivo data (left panel). The reverse analysis is depicted as a heatmap in the right panel.

bioRxiv preprint doi: https://doi.org/10.1101/368829; this version posted July 13, 2018. The copyright holder for this preprint (which was not certified by peer review) is the author/funder. All rights reserved. No reuse allowed without permission.

FIGURE 1

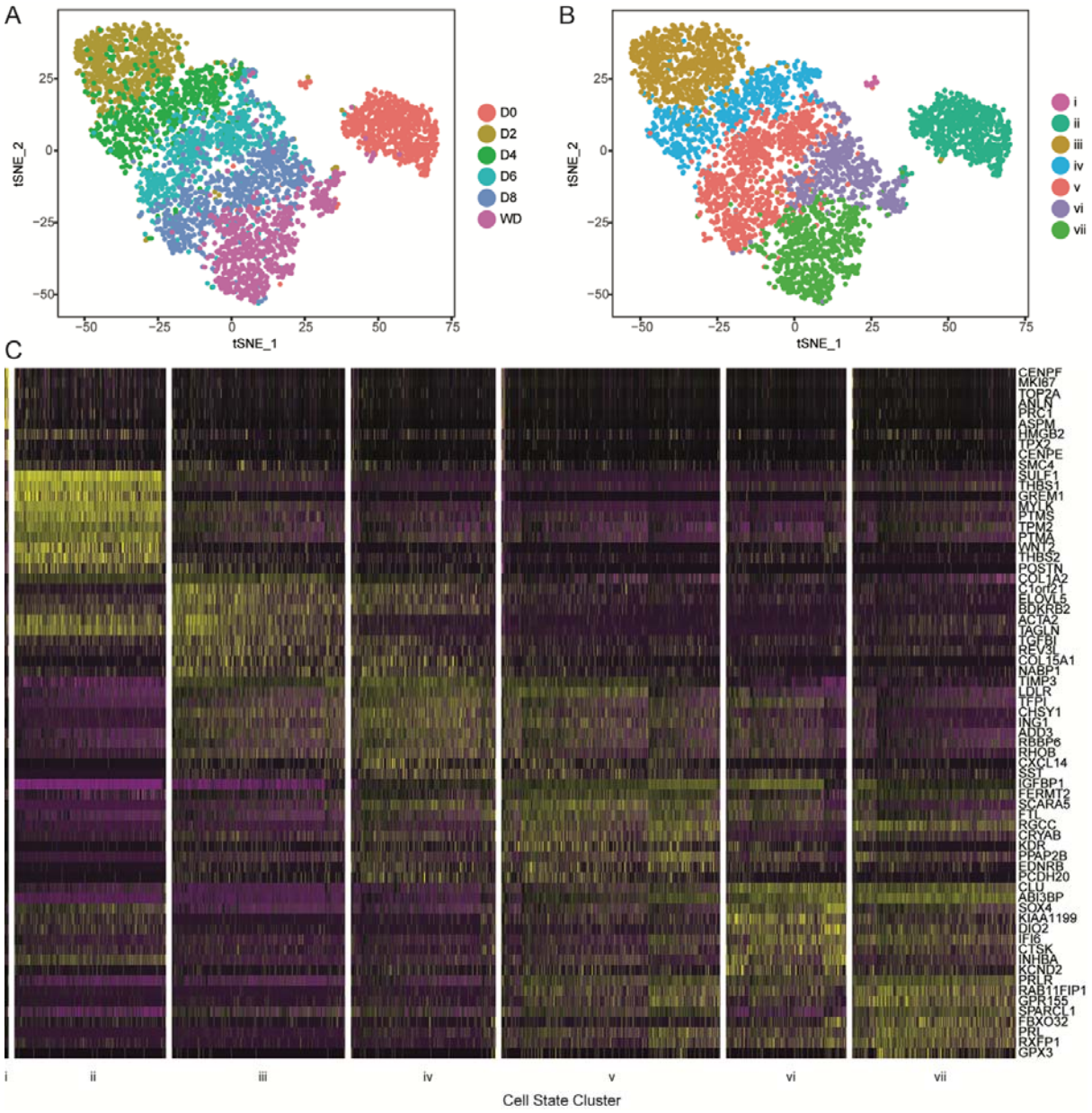

bioRxiv preprint doi: https://doi.org/10.1101/368829; this version posted July 13, 2018. The copyright holder for this preprint (which was not certified by peer review) is the author/funder. All rights reserved. No reuse allowed without permission.

FIGURE 2

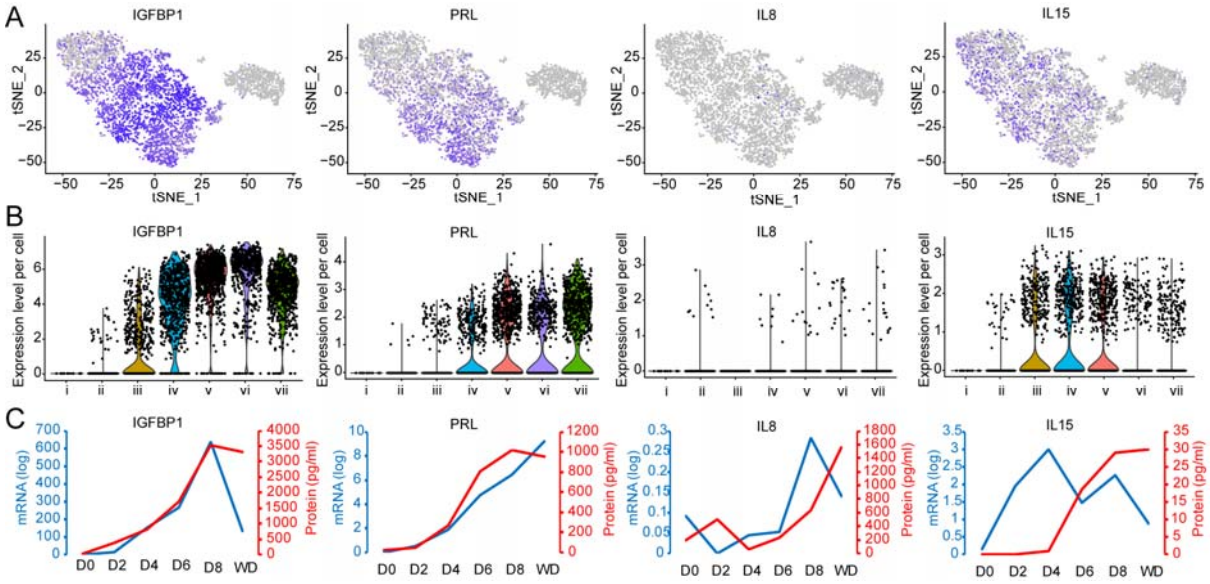

bioRxiv preprint doi: https://doi.org/10.1101/368829; this version posted July 13, 2018. The copyright holder for this preprint (which was not certified by peer review) is the author/funder. All rights reserved. No reuse allowed without permission.

FIGURE 3

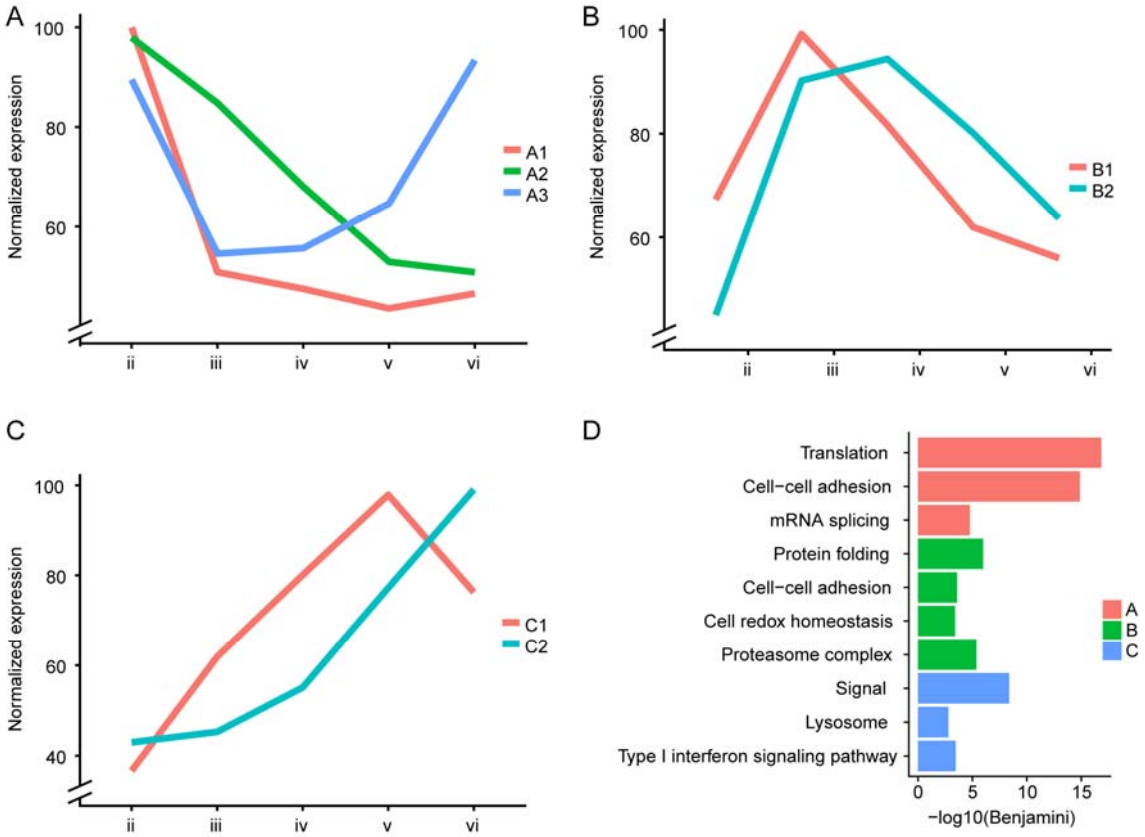

bioRxiv preprint doi: https://doi.org/10.1101/368829; this version posted July 13, 2018. The copyright holder for this preprint (which was not certified by peer review) is the author/funder. All rights reserved. No reuse allowed without permission.

FIGURE 4

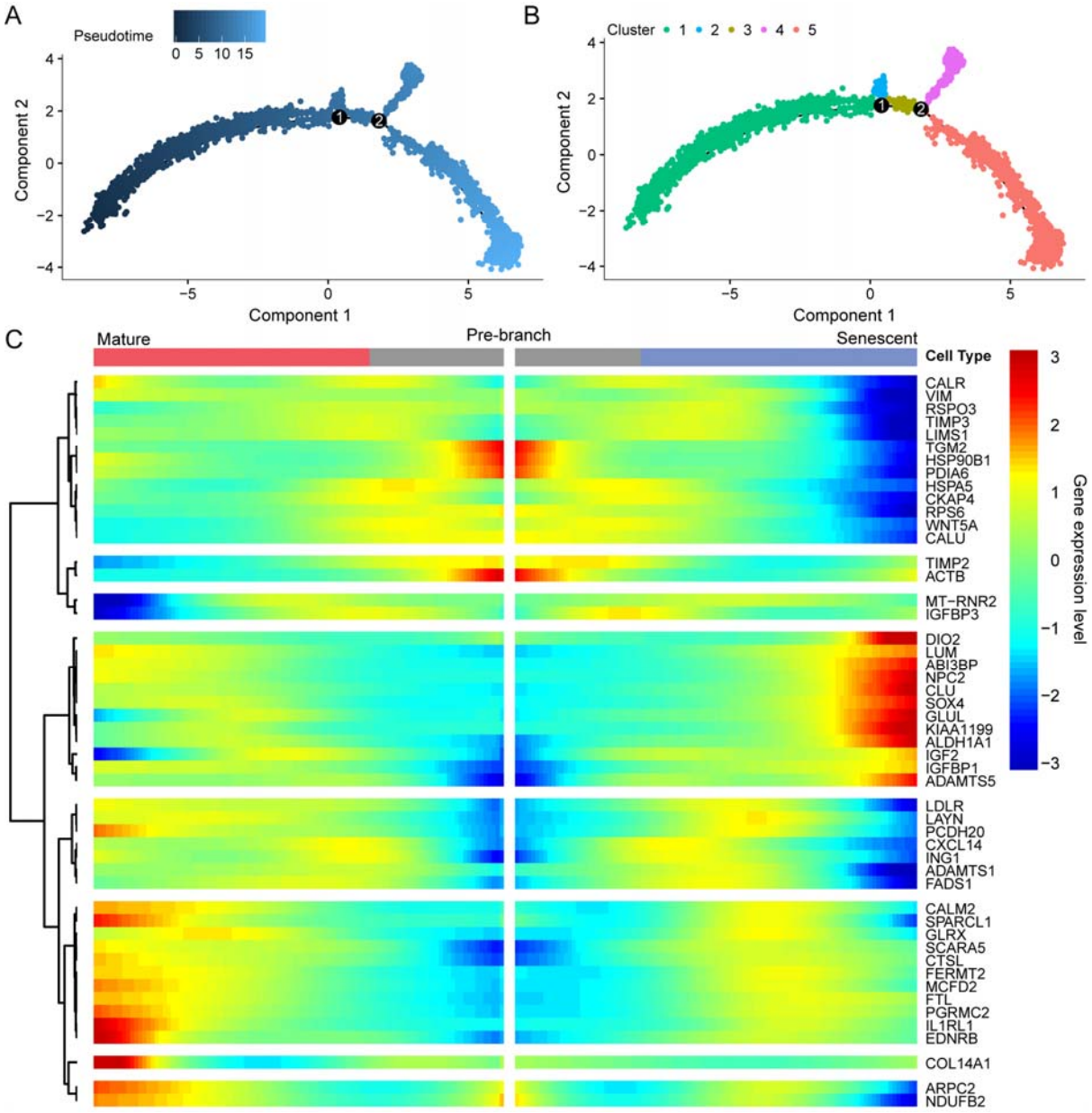

bioRxiv preprint doi: https://doi.org/10.1101/368829; this version posted July 13, 2018. The copyright holder for this preprint (which was not certified by peer review) is the author/funder. All rights reserved. No reuse allowed without permission.

FIGURE 5

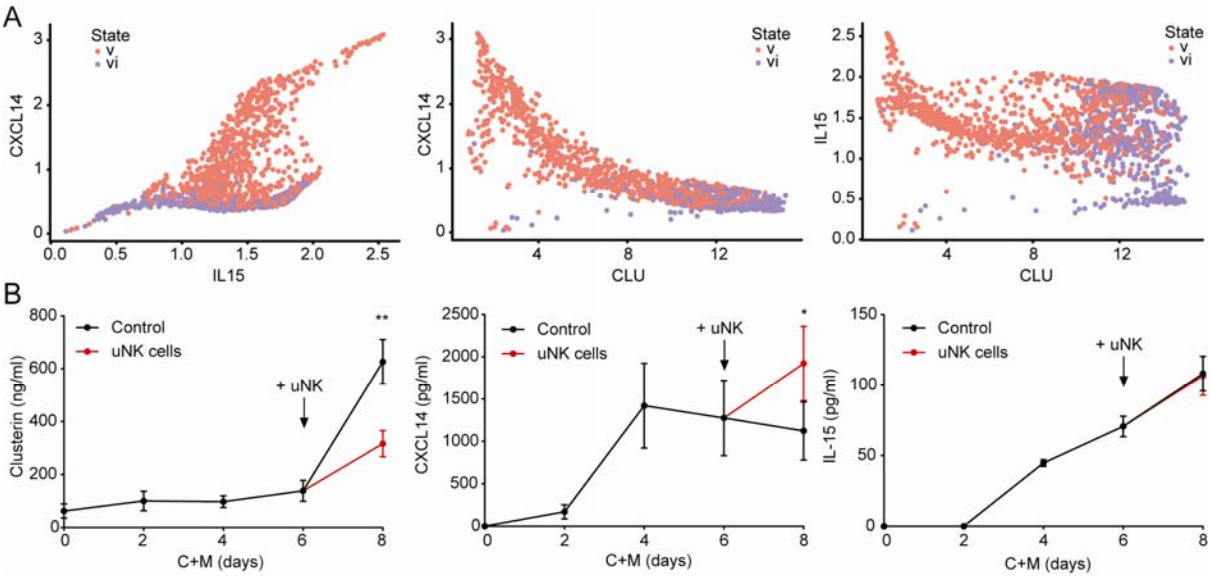

bioRxiv preprint doi: https://doi.org/10.1101/368829; this version posted July 13, 2018. The copyright holder for this preprint (which was not certified by peer review) is the author/funder. All rights reserved. No reuse allowed without permission.

FIGURE 6

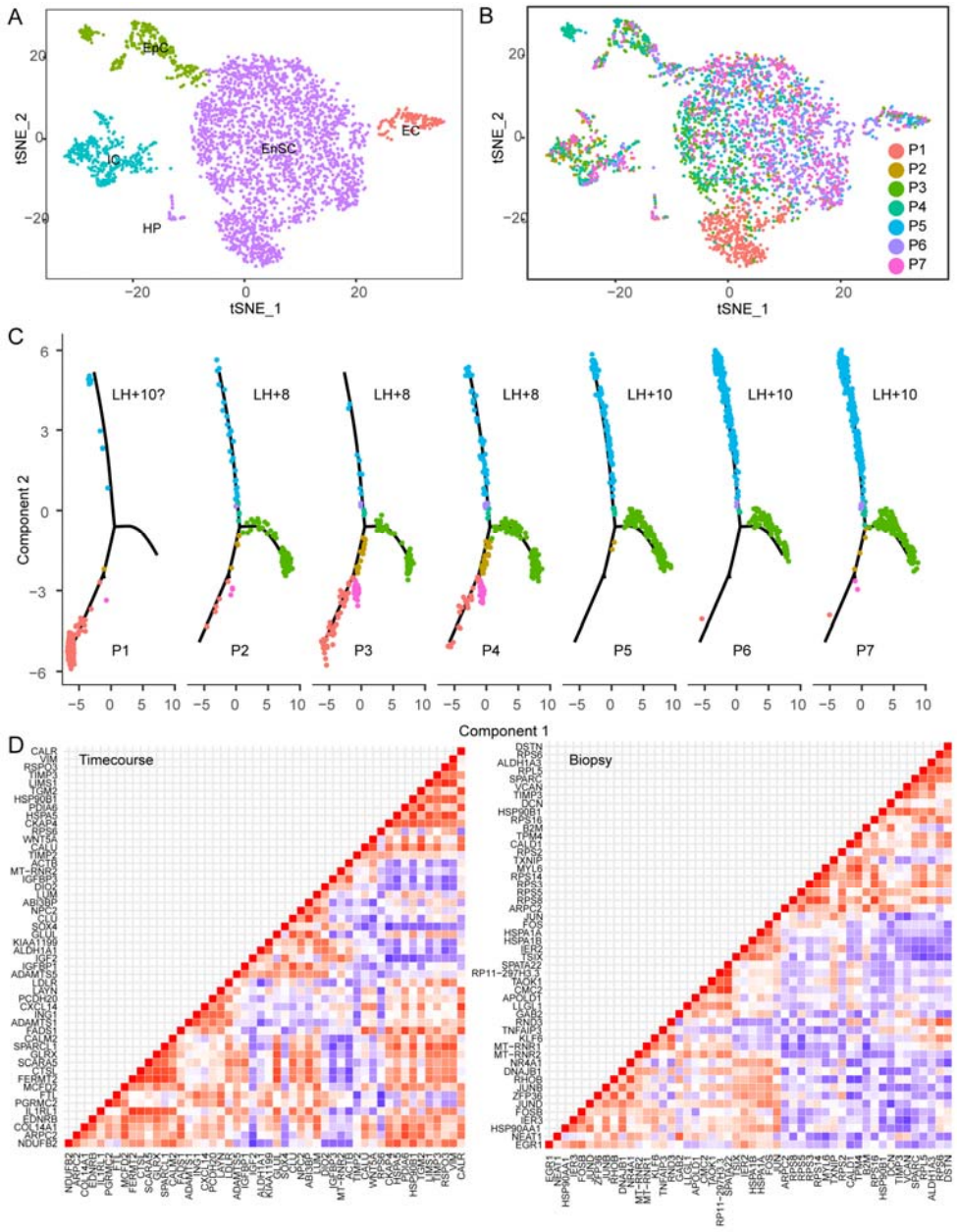

bioRxiv preprint doi: https://doi.org/10.1101/368829; this version posted July 13, 2018. The copyright holder for this preprint (which was not certified by peer review) is the author/funder. All rights reserved. No reuse allowed without permission.

SUPPLEMENTARY FIGURES

Reconstruction of the Decidual Pathways in Human Endometrial Cells Using Single-Cell RNA-Seq

Emma S Lucas, Pavle Vrljicak, Maria M Diniz-da-Costa, Paul J Brighton, Chow S Kong, Julia Lipecki, Katherine Fishwick, Joanne Muter, Sascha Ott, and Jan J Brosens

bioRxiv preprint doi: https://doi.org/10.1101/368829; this version posted July 13, 2018. The copyright holder for this preprint (which was not certified by peer review) is the author/funder. All rights reserved. No reuse allowed without permission.

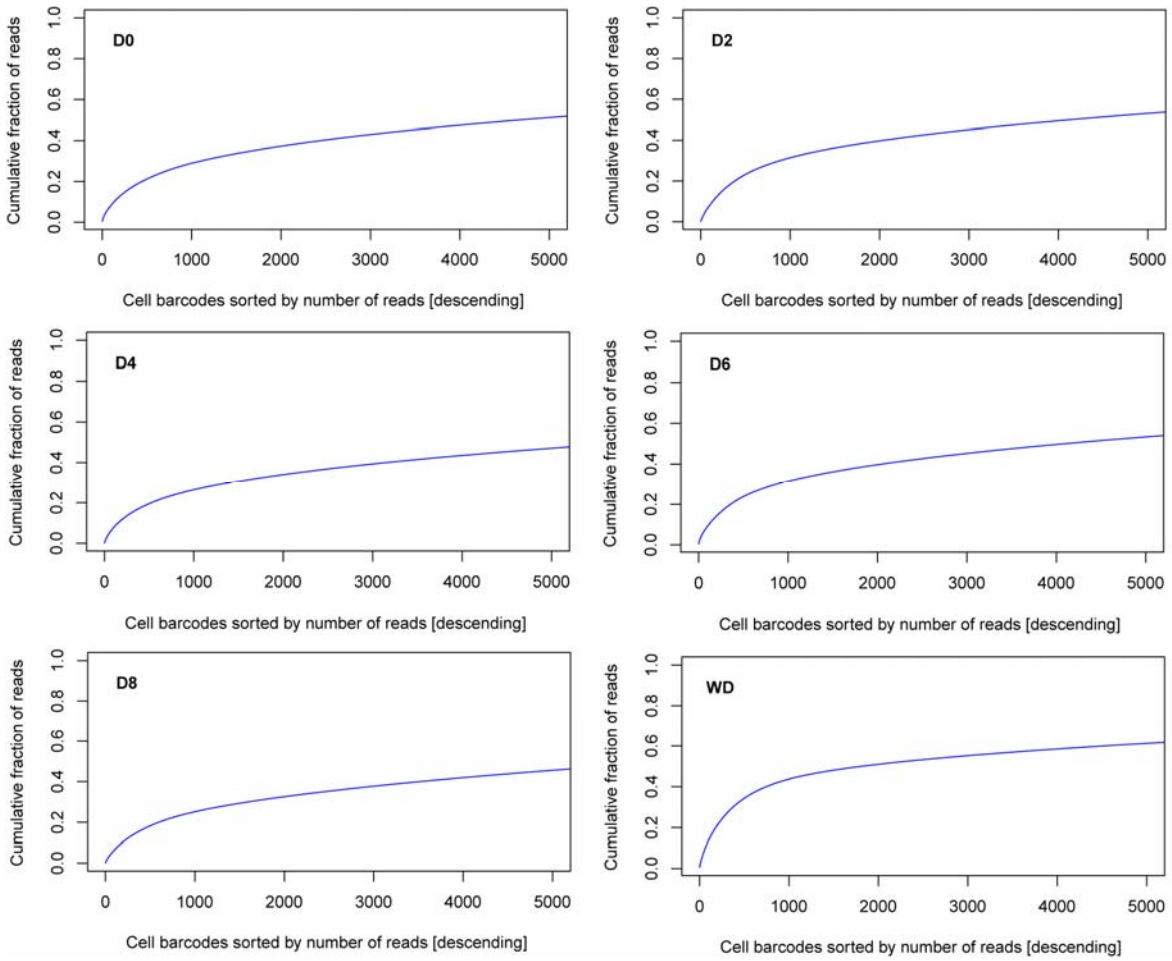

Figure S1. **Knee-plots of cumulative fraction of reads for time-course scRNA-seq libraries.** On the Y-axis is the cumulative fraction of total reads per captured cells. On the X-axis are the ordered cell barcodes based on total reads. The inflection point gives an estimate of the number of real cells.

bioRxiv preprint doi: https://doi.org/10.1101/368829; this version posted July 13, 2018. The copyright holder for this preprint (which was not certified by peer review) is the author/funder. All rights reserved. No reuse allowed without permission.

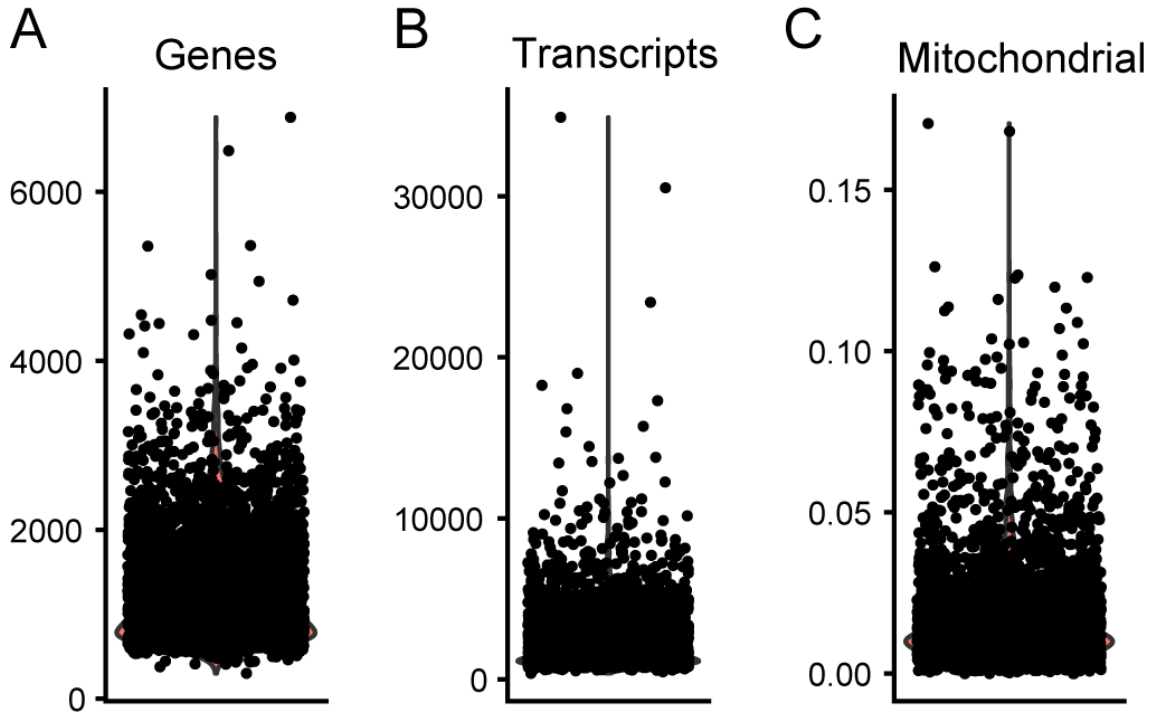

Figure S2. **Violin plots of number of genes.** (**A**), number of transcripts (**B**) and percent of mitochondrial genes per cell (**C**). Cells were included for further analysis if their number of genes ranged from 200 to 4500 and their proportion of mitochondrial genes did not exceed 5%.

bioRxiv preprint doi: https://doi.org/10.1101/368829; this version posted July 13, 2018. The copyright holder for this preprint (which was not certified by peer review) is the author/funder. All rights reserved. No reuse allowed without permission.

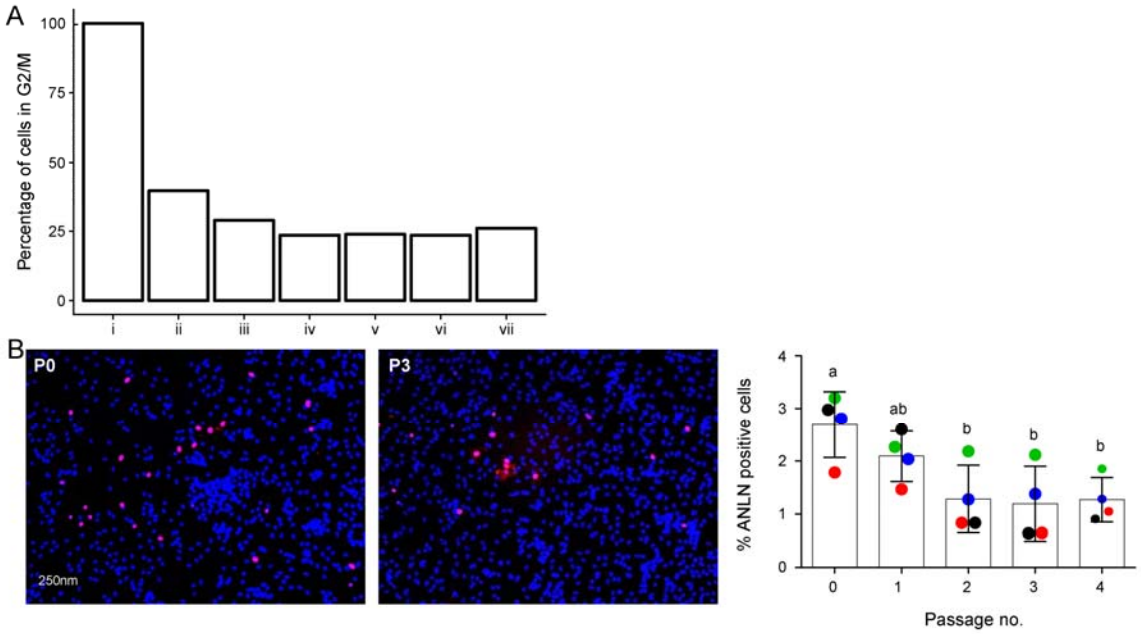

Figure S3. **Highly proliferative, anallin-positive EnSCs**. (**A**) Proportion of cells in each state that are in G2/M phase of the cycle. State *i* cells are exclusively of cells in G/2M phase of the cell cycle. (**B**) Representative immunofluorescent images showing anallin-positive cells in primary EnSC cultures at passage (P) 1 and 3 (left panel). Quantification of anallin (ANLN)-positive in P0-4 primary cultures (right panel).

bioRxiv preprint doi: https://doi.org/10.1101/368829; this version posted July 13, 2018. The copyright holder for this preprint (which was not certified by peer review) is the author/funder. All rights reserved. No reuse allowed without permission.

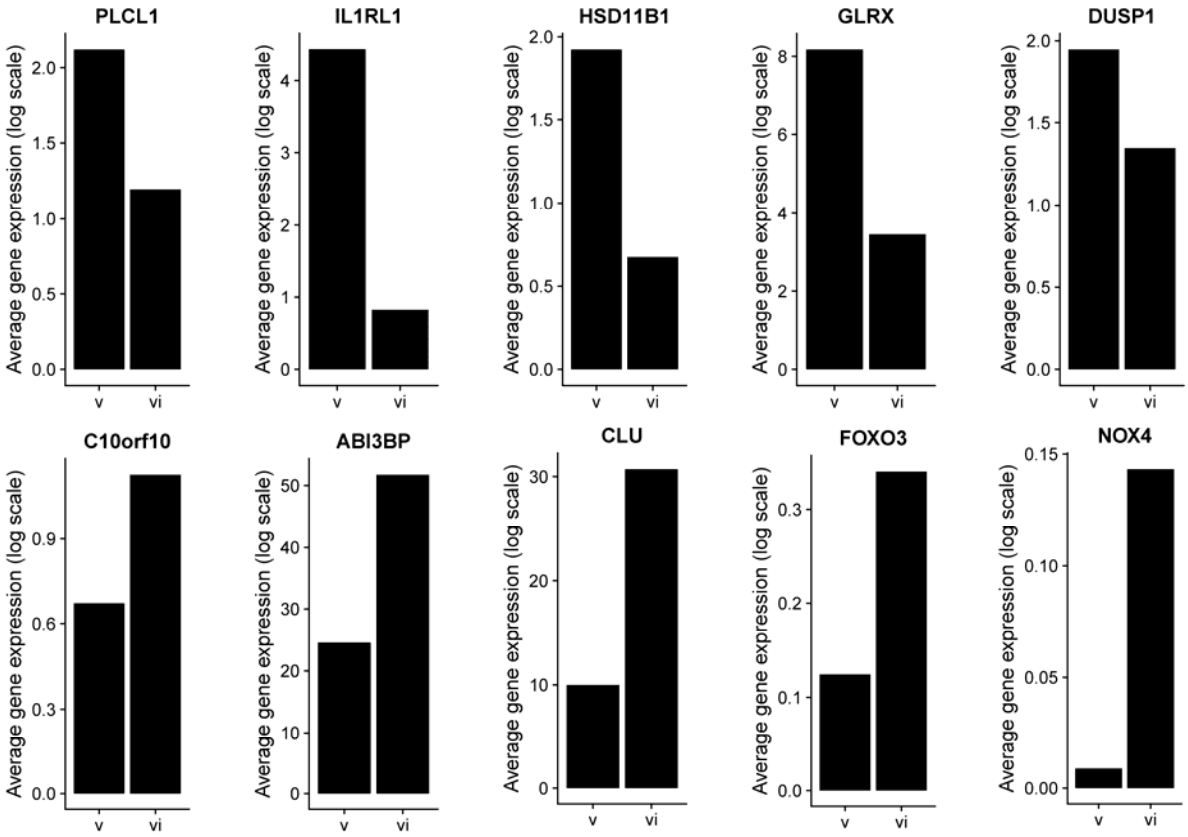

Figure S4. **Expression of genes involved in stress-resistance and oxidative stress/senescence in decidual subpopulations**. Bar-plots showing log-scaled average expression of specific genes, involved in decidual stress resistance (upper row) and oxidative stress/senescence (bottom row) in states *v* and *vi* cells.

bioRxiv preprint doi: https://doi.org/10.1101/368829; this version posted July 13, 2018. The copyright holder for this preprint (which was not certified by peer review) is the author/funder. All rights reserved. No reuse allowed without permission.

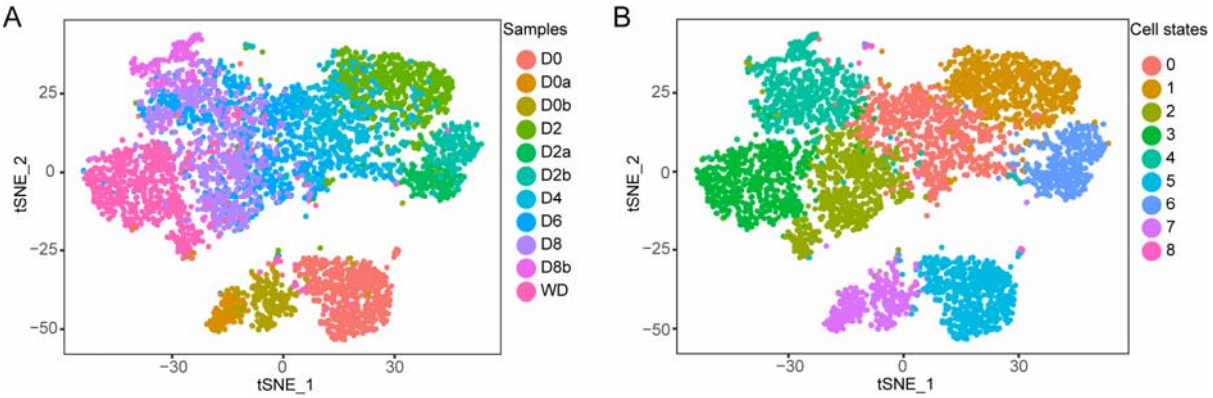

Figure S5. **Combined cell aggregation analysis of three independent primary cultures shows cells aggregating by state rather than sample**. (**A**) *t*-SNE plot with cells color-codes by culture and time of decidualization. (**B**) *t*-SNE plot with cells color-coded by cell state.

bioRxiv preprint doi: https://doi.org/10.1101/368829; this version posted July 13, 2018. The copyright holder for this preprint (which was not certified by peer review) is the author/funder. All rights reserved. No reuse allowed without permission.

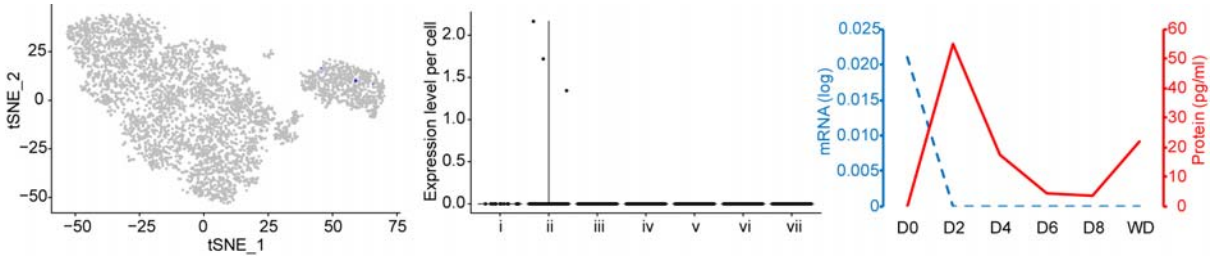

Figure S6. **Temporal expression and secretion of IL-6**. (**A**) Gene expression levels of *IL6* overlaid on *t*-SNE plot. Cells expressing specific genes are colored blue, with the color intensity reflecting the level of expression. (**B**) Violin plots showing relative levels of expression for *IL6* across the cell state clusters. (**C**) mRNA and secreted protein levels measured by ELISA in spent culture medium at indicated time-point by ELISA.

bioRxiv preprint doi: https://doi.org/10.1101/368829; this version posted July 13, 2018. The copyright holder for this preprint (which was not certified by peer review) is the author/funder. All rights reserved. No reuse allowed without permission.

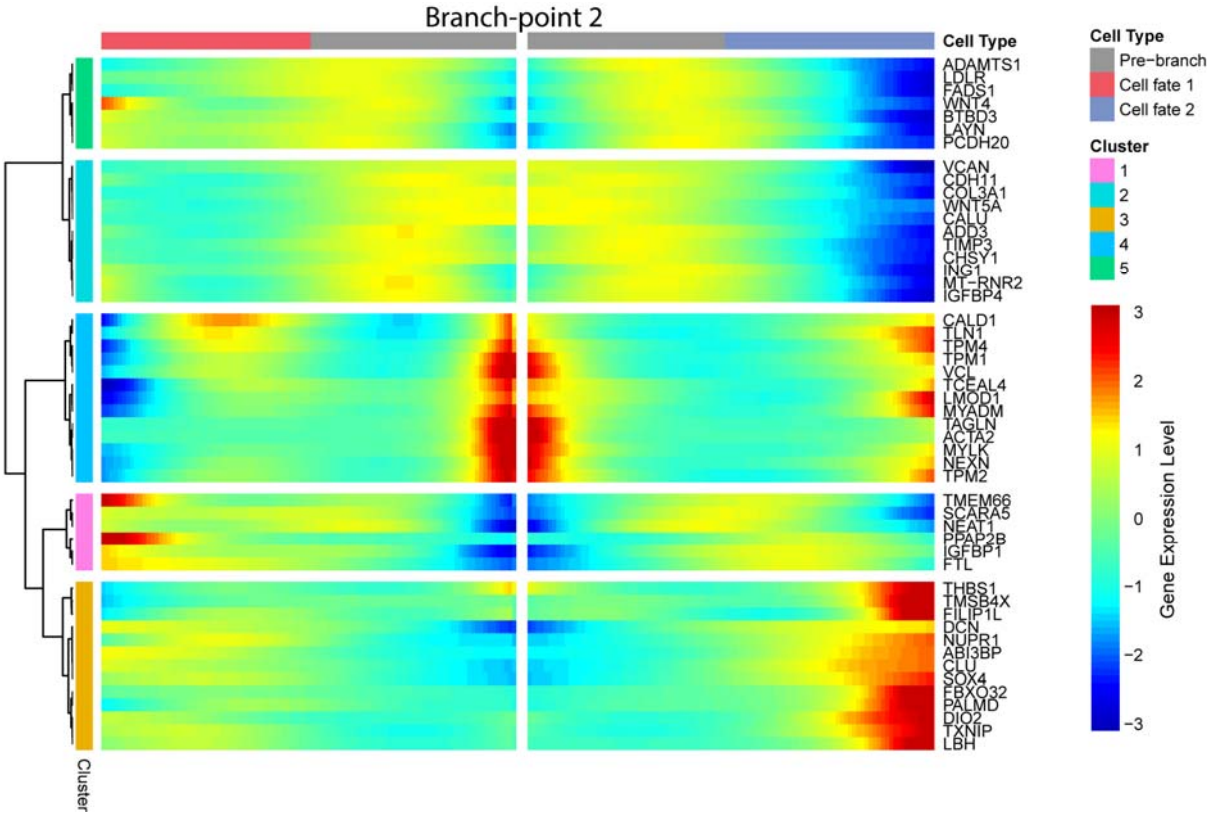

Figure S7. **Heatmap of top 50 genes distinguishing branch-point 2 in decidualizing EnSCs in culture**. Columns are points in pseudotime while rows represent the 50 most dynamic genes at this branch-point. Hierarchical clustering visualizes modules of genes with similar lineage-dependent expression patterns.

bioRxiv preprint doi: https://doi.org/10.1101/368829; this version posted July 13, 2018. The copyright holder for this preprint (which was not certified by peer review) is the author/funder. All rights reserved. No reuse allowed without permission.

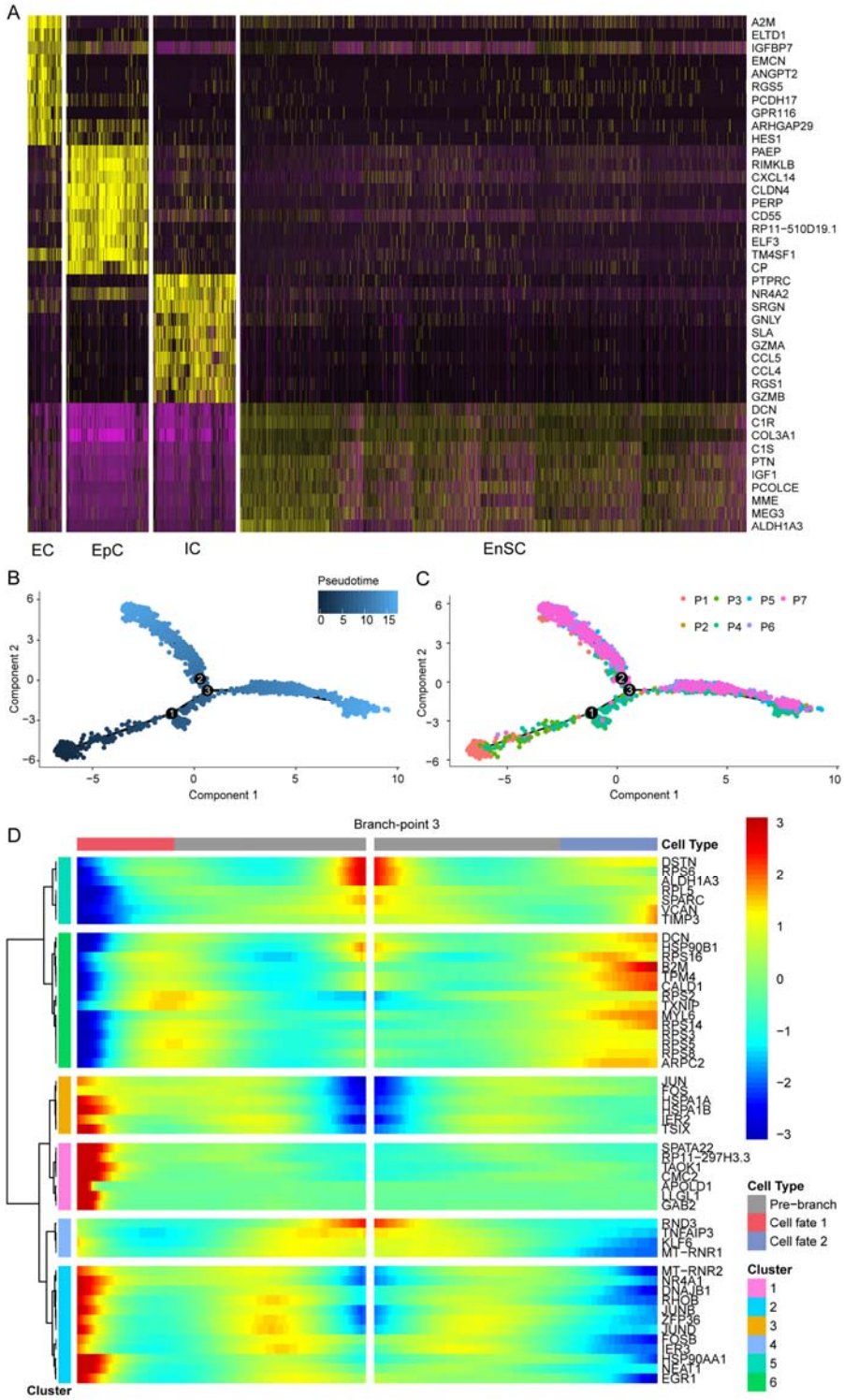

Figure S8. **Cell aggregation analysis of biopsy data.** (**A**) Heatmap of marker genes from *t*-SNE plot in Figure 6A. (**B**) Cells coloured by pseudotime. Two minor branch-points (designated 1 and 2) and the major branch-point (designated 3) are indicated. (**C**) Cells coloured by sample. (**D**) Heatmap top 50 genes distinguishing branch-point 3.

bioRxiv preprint doi: https://doi.org/10.1101/368829; this version posted July 13, 2018. The copyright holder for this preprint (which was not certified by peer review) is the author/funder. All rights reserved. No reuse allowed without permission.

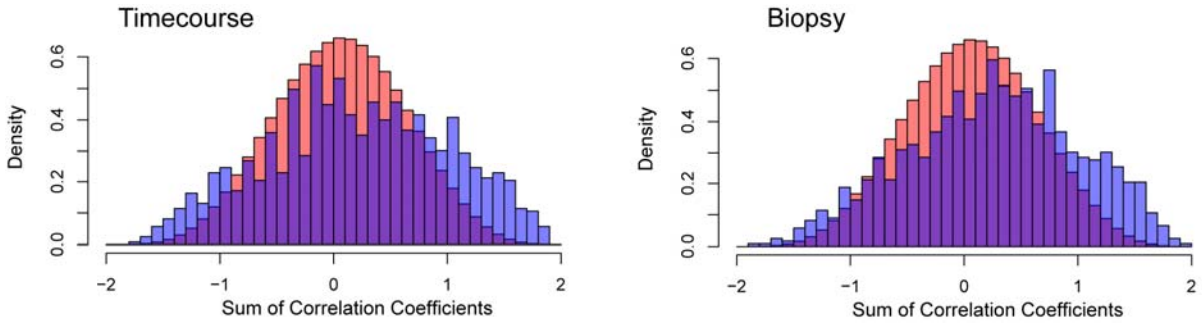

Figure S9. **Histogram of sum of correlation coefficients for time-course and biopsy branch-points**.

bioRxiv preprint doi: https://doi.org/10.1101/368829; this version posted July 13, 2018. The copyright holder for this preprint (which was not certified by peer review) is the author/funder. All rights reserved. No reuse allowed without permission.

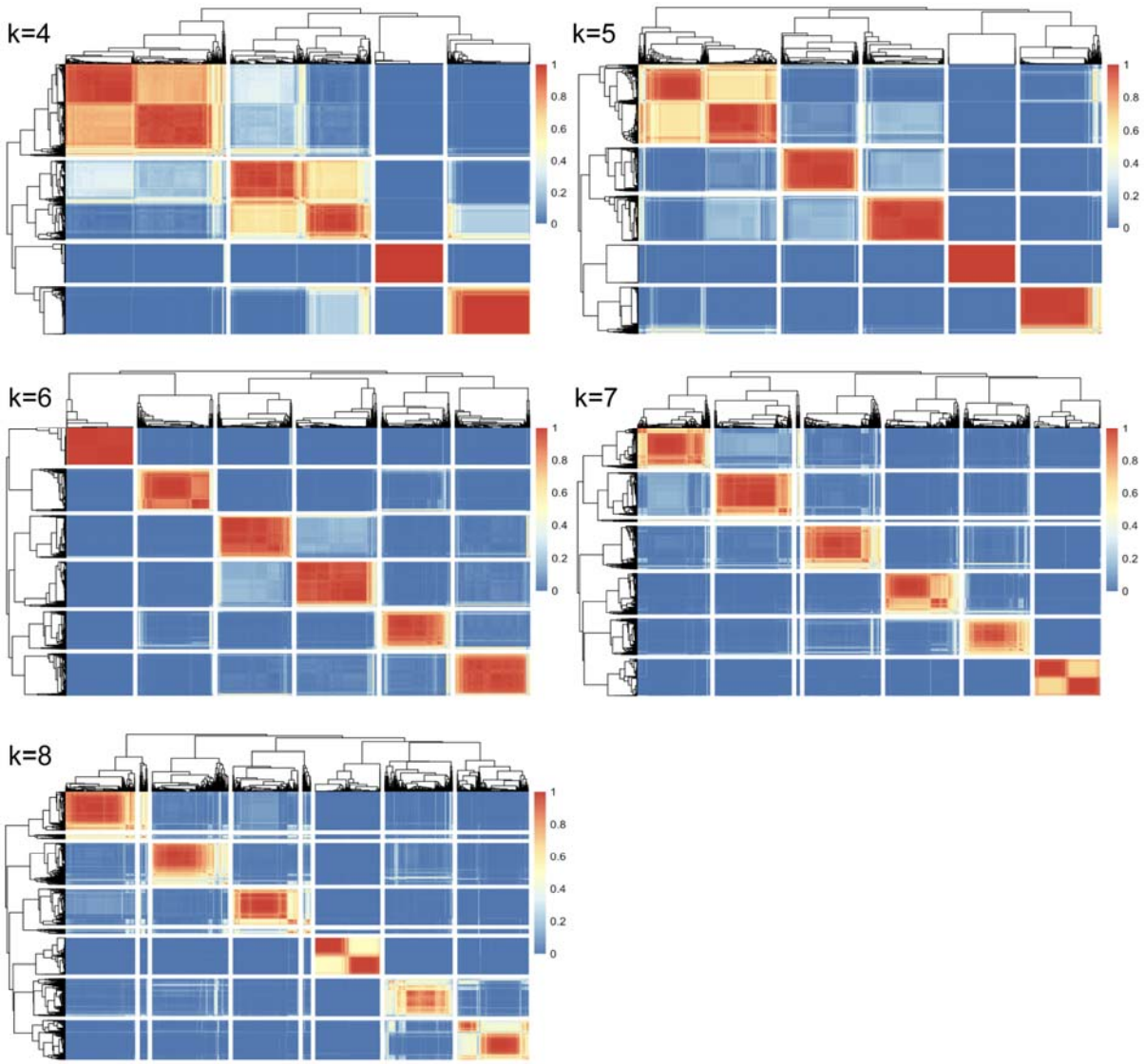

Figure S10: **Consensus clustering results using SC3 for k=4 to k=8.**